ACS OMEGA

http://pubs.acs.org/journal/acsodf

Article

Wafer-Scale Fabrication of Silicon Nanocones via Controlling Catalyst Evolution in All-Wet Metal-Assisted Chemical Etching

Chenyu Bian, Bingchang Zhang,* Zhenghe Zhang, Hui Chen, Dake Zhang, Shaojun Wang, Jing Ye, Le He, Jiansheng Jie,* and Xiaohong Zhang*

Cite This: *ACS Omega* 2022, 7, 2234−2243

Read Online

ACCESS | Metrics & More | Article Recommendations | Supporting Information

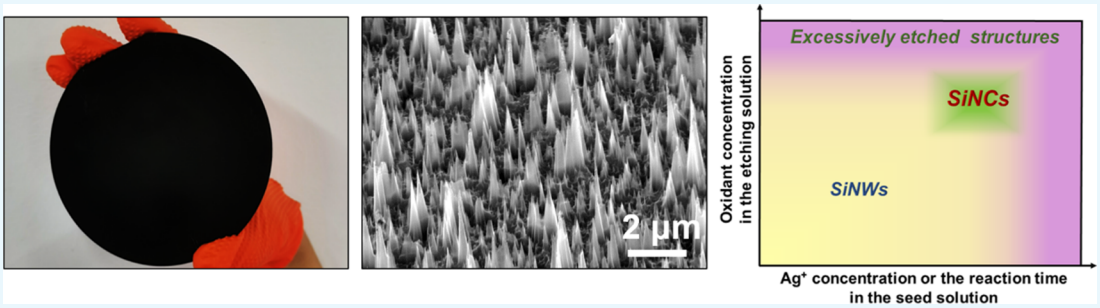

ABSTRACT: All-wet metal-assisted chemical etching (MACE) is a simple and low-cost method to fabricate one-dimensional Si nanostructures. However, it remains a challenge to fabricate Si nanocones (SiNCs) with this method. Here, we achieved wafer-scale fabrication of SiNC arrays through an all-wet MACE process. The key to fabricate SiNCs is to control the catalyst evolution from deposition to etching stages. Different from conventional MACE processes, large-size Ag particles by solution deposition are obtained through increasing $AgNO_3$ concentration or extending the reaction time in the seed solution. Then, the large-size Ag particles are simultaneously etched during the Si etching process in an etching solution with a high H_2O_2 concentration due to the accelerated cathode process and inhibited anode process in Ag/Si microscopic galvanic cells. The successive decrease of Ag particle sizes causes the proportionate increase of diameters of the etched Si nanostructures, forming SiNC arrays. The SiNC arrays exhibit a stronger light-trapping ability and better photoelectrochemical performance compared with Si nanowire arrays. SiNCs were fabricated by using n-type 1−10 Ω cm Si(100) wafers in this work. Though the specific experimental conditions for preparing SiNCs may differ when using different Si wafers, the summarized diagram will still provide valuable guidance for morphology control of Si nanostructures in MACE processes.

INTRODUCTION

One-dimensional (1D) silicon nanostructures including silicon nanowires (SiNWs),[1,2] silicon nanocones (SiNCs),[3−5] and silicon nanopores[6] have been intensively studied for optoelectronic applications due to their characteristics of strong light trapping,[7,8] radial carrier separation,[9] and large surface-to-volume ratios.[10] Among various 1D silicon nanostructures, SiNCs have attracted special attention. SiNCs not only possess the normal advantages of 1D silicon nanostructures but also have some unique merits: (i) the light absorption of SiNCs is insensitive to incident angles.[11] Compared to planar Si and other Si nanostructure arrays, SiNC arrays exhibit superior antireflection properties over a large range of incident angles, which is significant for practical solar conversion applications and omnidirectional photodetectors.[12−14] (ii) It is easier to perform surface passivation, heterojunction construction, and catalyst loading in SiNC arrays than in other Si nanostructure arrays because of the large openings and nonvertical sidewalls of SiNCs.[15−17] (iii) SiNCs are promising in self-cleaning surfaces[18] and field emission,[4,19] due to the unique cone structures.

Encouraged by the excellent properties and the promising application prospects of SiNCs, considerable efforts have been devoted to SiNC fabrication to promote their research and practical applications. For example, SiNCs can be fabricated through reactive ion etching by using arranged nanoparticles, such as polystyrene spheres,[18] SiO_2 particles,[11,20−22] or silicon oxybromide nanohemispheres,[23] as masks. During the etching process, the radii of the nanoparticles were continuously changed, which further caused the diameter change of the etched silicon nanostructures, enabling the formation of

Received: October 16, 2021
Accepted: December 23, 2021
Published: January 4, 2022

https://doi.org/10.1021/acsomega.1c05790
ACS Omega 2022, 7, 2234−2243

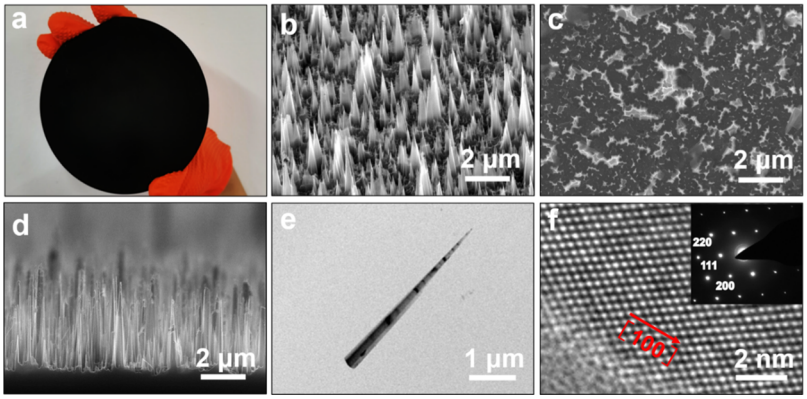

Figure 1. Wafer-scale fabrication of SiNCs through diameter control in an all-wet MACE process. (a) Photograph of a 4 in. Si wafer covered with SiNC arrays. (b–d) 45° oblique-view, top-view, and sectional-view SEM images of SiNC arrays, respectively. (e) TEM image of an individual SiNC. (f) HRTEM image of an individual SiNC. The inset shows the corresponding SAED pattern.

SiNCs. Moreover, SiNCs can also be obtained through radial growth[24] or catalyst shrinking effect[25,26] in a vapor–liquid–solid (VLS) growth process. However, the masked dry etching process is complexed and normally limited to small areas, while VLS growth usually needs a high-temperature process. Thus, it is very desirable to develop a facile and low-cost method for large-scale fabrication of SiNCs.

Metal-assisted chemical etching (MACE) is a well-known approach for fabricating 1D Si nanostructures.[27] It usually consists of two basic steps, though it may have different experimental details. First, metal catalysts are deposited on the surface of Si wafers through magnetron sputtering,[28] thermal evaporation,[29] electron beam (e-beam) evaporation,[30] or solution deposition.[31] Then, Si wafers with metal catalysts are etched in an etching solution containing oxidants and HF to obtain 1D Si nanostructures. Among different MACE methods, the all-wet MACE process with solution deposition of catalysts is especially attractive due to its merits of simplicity, high efficiency, low cost, and suitability for mass production, which has been successfully applied in the solar industry for constructing an anti-reflection surface.[32,33] Despite the great potential of this method in applications, it is still hard to fabricate SiNCs through the all-wet MACE method due to the insufficient diameter-control investigations. In addition, current research studies on morphology control in MACE mainly focus on regulating the etching process.[34−36] Investigations on the Ag deposition process are lagging behind, which may bring new chances for morphology-controlled fabrication of 1D Si nanostructures.

Herein, wafer-scale fabrication of SiNC arrays was achieved in an all-wet MACE process through controlling catalyst evolution from deposition to etching stages. The solution-deposition process of Ag particles is particularly studied. It is found that sizes of Ag particles can be obviously increased by extending reaction time or increasing reactant concentration in the seed solution. Ag particles with relatively large diameters are a necessary condition for fabricating SiNCs. In optimal experiment for fabricating SiNCs, the average diameters of Ag particles are in the range from 100 to 500 nm, with an average value of 370 nm. In an etching solution with a high H_2O_2 concentration, the Ag particles will continuously decrease along with the etching of Si due to an extra anode reaction of Ag etching. The size reduction of the Ag particles caused the proportionate increase of the diameter of Si nanostructures to form SiNCs. Based on the experiment and reported results, a diagram showing the relationship between the morphology of Si nanostructures and reaction conditions was summarized. Finally, the light absorption of SiNC arrays was measured as 95.9–98.2% in the visible range (400–780 nm). Our work opens a new avenue to control the morphologies and structures of Si nanostructures for high-performance optoelectronic devices.

RESULTS AND DISCUSSION

Wafer-Scale Fabrication of SiNCs. With optimum conditions, wafer-scale fabrication of SiNCs was successfully achieved through controlling catalyst deposition and evolution in the all-wet MACE process. First, a clean 4 in. Si wafer was immersed in a seed solution composed of 0.02 M $AgNO_3$ and 4.8 M HF for 120 s. Then, the Si wafer was transferred into an etching solution composed of 0.4 M H_2O_2 and 4.8 M HF and etched for 15 min. Finally, the Si wafer was soaked in 65% HNO_3 to remove Ag catalysts and rinsed with deionized water. A black Si wafer was obtained (Figure 1a). Scanning electron microscopy (SEM) characteristics show that vertically standing SiNC arrays with a height around 3 μm uniformly cover the whole Si wafer (Figure 1b–d). The morphology and optical property through the whole wafer are basically consistent (Figure S1). Energy-dispersive X-ray (EDX) analysis shows no Ag peaks after dealt with 65% HNO_3 (Figure S2), indicating low-level Ag residual below the detection limit of EDX. Figure 1e shows the typical transmission electron microscopy (TEM) image of a SiNC removed from the substrate, which displays the tapered structure. High-resolution TEM (HRTEM) and selected-area electron diffraction (SAED) show the single-crystal nature and the [100] axial crystallographic orientation of SiNCs, consistent with the original Si wafer (Figure 1f). Moreover, the cone angle is measured in the range of 5.4–7.3° (Figure S3). The small and variable cone angle implies that the etching direction is along different high-index crystallographic orientations, which indicates that the etching of SiNCs is not dominant by specific crystal orientation.

It is noteworthy that reports on fabricating SiNCs directly through an all-wet MACE method are absent up to date. Though some literatures have reported various Si nanostructures with low reflectivity by using the all-wet MACE method, their morphologies and experimental parameters are very different from SiNCs in this work.[37−42] The key parameters for SiNC fabrication were further revealed through contrastive studies as given below.

https://doi.org/10.1021/acsomega.1c05790
ACS Omega 2022, 7, 2234−2243

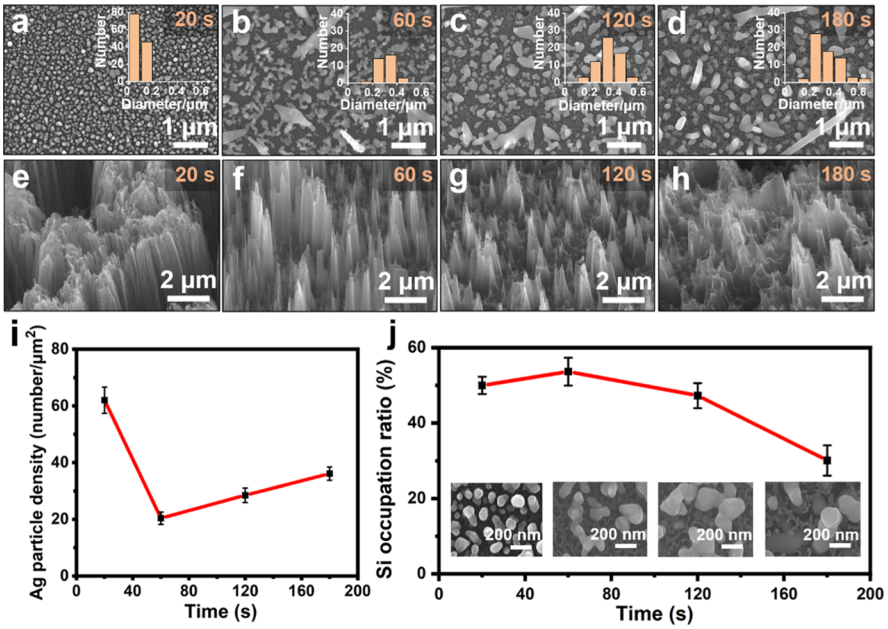

Figure 2. Effect of Ag deposition time on the morphologies of Si nanostructures. (a–d) Top-view SEM images of Si wafers after reaction in seed solution for 20, 60, 120, and 180 s, respectively. Inset diagrams plot corresponding size distributions of the Ag particles on the surfaces of 2 μm^2 Si substrates. (e–h) 45° oblique-view SEM images of corresponding Si nanostructures obtained by etching the sample (a–d) in the etching solution for 15 min. (i) Relationship between the Ag particle density on the surface of the Si substrate and Ag depositing time. (j) Relationship between the Si occupation ratio and Ag depositing time.

Effect of Ag Deposition Conditions on the Morphologies of Si Nanostructures. The reaction time of Si wafers in the aqueous solution of 0.02 M $AgNO_3$ and 4.8 M HF was first regulated to study its effect on the morphology of etched Si nanostructures. The samples after deposition of Ag particles were characterized with SEM. Intuitively, the diameters of Ag particles gradually increase, as the deposition time extends (Figure 2a–d). The sizes and density of Ag particles on the surfaces of the substrates were statistically investigated to understand their evolution. With a short deposition time of 20 s, the diameters of Ag particles are no more than 200 nm with a relatively uniform distribution (inset in Figure 2a). As the deposition time extends, the diameters of Ag particles gradually increase with a wider size distribution (insets in Figure 2b–d), while the density of Ag particles on the surface first decreases and then increases (Figure 2i). The number evolution can be understood by analyzing the action of Ag particles. When the deposition time increases, the existing Ag particles will gradually drill into the substrate and some new Ag particles will be produced (Figure 2j inset). The density of Ag particles decreases, as the deposition time increases from 20 to 60 s due to the leading role of drilling. When the deposition time increases from 60 to 180 s, the production of new Ag particles is the main reason for the increasing density of Ag particles. The abovementioned analyses provide a detailed picture of the evolution of Ag particles for rationally controlling their size and number.

Different size distributions of Ag particles can result in different Si nanostructures in the etching process (Figure 2e–h). When the abovementioned samples reacted in an etching solution of 0.4 M H_2O_2 and 4.8 M HF for 15 min, different Si nanostructures were obtained. The sample with 20 s Ag deposition is SiNWs because small-size Ag particles are not etched along with the etching of Si. In contrast, the sample with 120 s Ag deposition is fine SiNCs due to the simultaneous etching of large-size Ag particles and Si. Moreover, the sample with 180 s Ag deposition is found excessively etched owing to the excessive Ag deposition. These results indicate that large Ag particles obtained by solution deposition can effectively catalyze the fabrication of SiNCs, while small ones can merely induce SiNW formation.

In addition, it is found that the density of final Si nanostructures becomes smaller, as Ag deposition time extends. A parameter called Si occupation ratio was proposed to explain the density evolution. From the SEM images of samples after Ag deposition, three different morphologies including etched holes, unetched Si, and Ag particles can be observed (Figure S4). The Si occupation ratio is defined as the ratio of the unetched Si area to the image area. On the whole, the Si occupation ratio decreases with the increase of Ag deposition time due to the continuous production of Ag particles and etching of Si (Figure 2j). Because unetched Si after Ag deposition corresponds to the final Si nanostructures, the etched nanostructures become sparser until excessively etched, as the Si occupation ratio decreases (Figure 2e–h). Note that the Si occupation ratio after 20 s Ag deposition is slightly smaller than that after 60 s Ag deposition, which may be attributed to the shelter of the Si substrate by dense and increased Ag particles at a short deposition time of 20 s (Figure S5). These results imply that the density of Si nanostructures can also be modulated through controlling the Ag deposition process.

Furthermore, the effect of $AgNO_3$ concentration on the morphologies of Si nanostructures was also investigated. When the $AgNO_3$ concentration was reduced by half (0.01 M) and the reaction time was 120 s, SiNWs were obtained (Figure S6), similar to the case with the $AgNO_3$ concentration of 0.02 M and the reaction time of 20 s. When the $AgNO_3$ concentration was 0.01 M and the reaction time was extended to 240 s, SiNCs were obtained (Figure S7), similar to the case with the

https://doi.org/10.1021/acsomega.1c05790
ACS Omega 2022, 7, 2234–2243

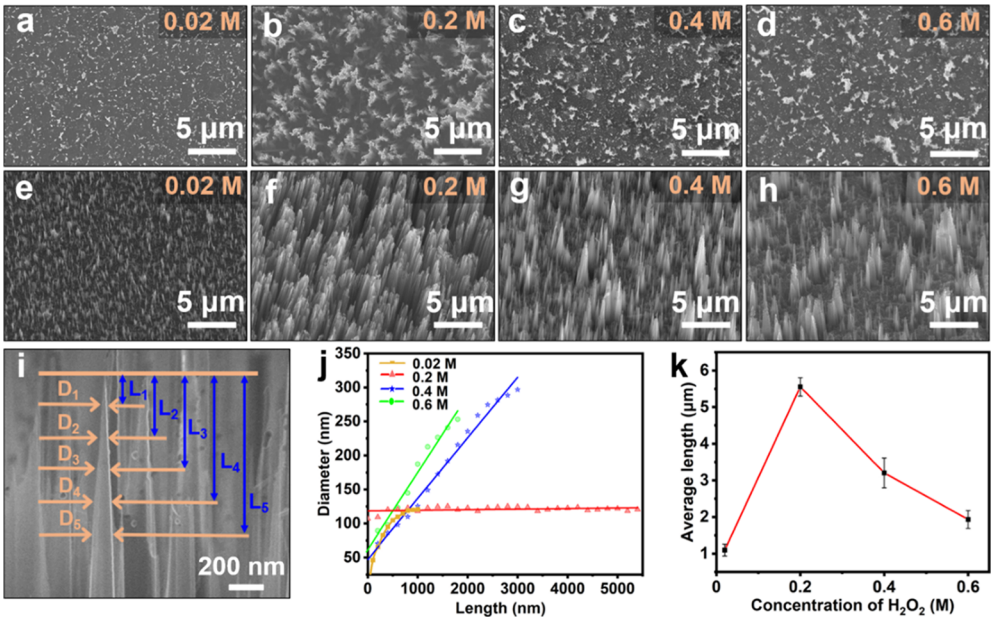

Figure 3. Effect of H_2O_2 concentration on the morphologies of Si nanostructures. (a–d) Top-view SEM images and (e–h) 45° oblique-view SEM images of Si nanostructures etched in etching solution with H_2O_2 concentrations of 0.02, 0.2, 0.4, and 0.6 M, respectively. (i) Measurement diagram of length and diameter of Si nanostructures. (j) *L*–*D* relationship of typical Si nanostructures etched in solution with different H_2O_2 concentrations. (k) Relationship between the length of Si nanostructures and H_2O_2 concentration.

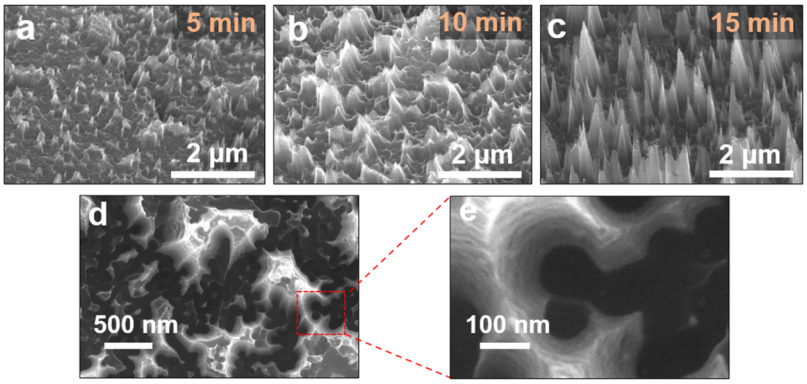

Figure 4. Forming processes of SiNCs. (a–c) 45° oblique-view SEM images of Si nanostructures etched in 0.4 M H_2O_2/4.8 M HF solution for 5, 10, and 15 min, respectively. (d,e) Close-up top-view SEM images of SiNCs and inverted conic holes.

$AgNO_3$ concentration of 0.02 M and the reaction time of 120 s. These results indicate that when $AgNO_3$ concentration decreases, the same morphologies of Si nanostructures can be obtained through extending the reaction time in the seed solution. Hence, increasing $AgNO_3$ concentration and extending the reaction time in the seed solution have the same effect on the morphology of etched Si nanostructures. This is because both parameters will determine the size and density of Ag particles following similar rules.

Effect of Catalyst Evolution in the Etching Process on the Morphologies of Si Nanostructures. Another key parameter that may affect catalyst evolution and thus SiNC formation is the oxidant concentration. H_2O_2 concentrations of 0.02, 0.2, 0.4, and 0.6 M in the etching solution were chosen to study their effects on the morphologies of etched Si nanostructures. A constant reaction time of 120 s in seed solution of 0.02 M $AgNO_3$ and 4.8 M HF and a constant reaction time of 15 min in etching solution were set to conduct the controlled experiments. It is observed that the morphology of Si nanostructures strongly depends on the H_2O_2 concentration (Figure 3a–h). The relationship between length (L) and diameter (D) of etched Si nanostructures was quantitatively studied to precisely analyze their morphologies. As shown in Figure 3i, the diameter was measured every 200 nm length. In each reaction condition, the *L*–*D* plots of measured samples possess similar slopes but different intercepts (Figure S8). The different intercepts could be attributed to the random Si occupation areas between Ag particles before etching (Figure S9). The typical *L*–*D* relationship from different samples is exhibited in Figure 3j. When the H_2O_2 concentration is low (*e.g.*, 0.02 M), short SiNCs were formed due to the slow and conformal etching along the circular edge of Ag particles. At a H_2O_2 concentration of 0.2 M, the nanostructures are SiNWs with uniform diameters. When the H_2O_2 concentration increases to 0.4 M or 0.6 M, the diameter of nanostructures changes with their length, forming SiNCs. However, SiNCs etched at the H_2O_2 concentration of 0.6 M are sparser and shorter than those of 0.4 M, implying some excessive etching at a solution with a very high H_2O_2 concentration (Figure 3k).

https://doi.org/10.1021/acsomega.1c05790
ACS Omega 2022, 7, 2234–2243

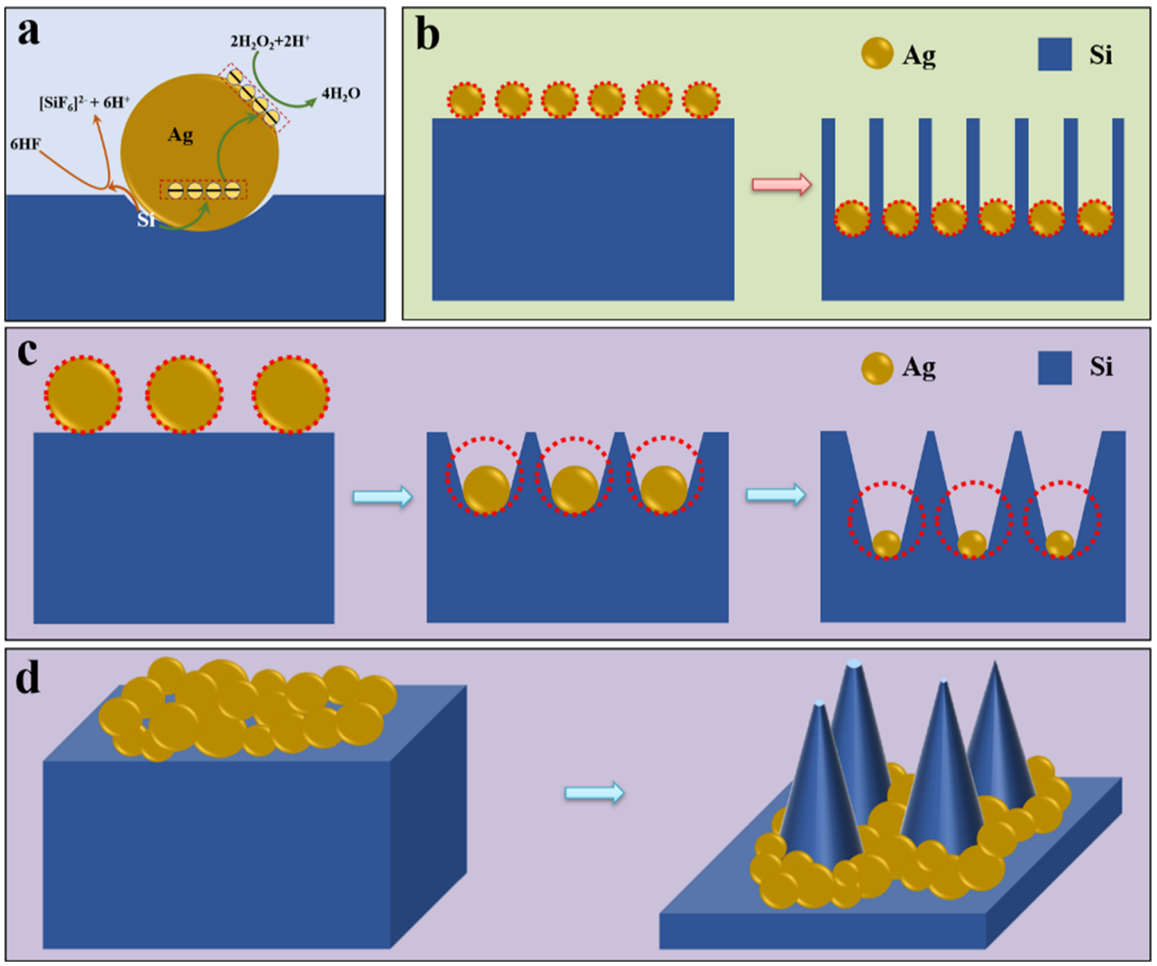

Figure 5. Schematic diagrams of the reaction mechanism and morphology control in MACE. (a) Schematic of chemical processes involved in the MACE process. (b) Schematic illustration of the formation process of SiNWs. (c) Schematic illustration of the formation process of inverted conic holes. (d) Schematic illustration of the formation process of SiNCs.

Forming Processes of SiNCs. According to the above-mentioned observations, solution deposition of large-size Ag particles and an appropriately high H_2O_2 concentration are necessary conditions for all-wet MACE fabrication of SiNCs. Furthermore, we investigated the forming processes of SiNCs in the experiment to reveal the mechanism. The experiments were conducted through reacting in a seed solution with 0.02 M $AgNO_3$ and 4.8 M HF for 120 s and then etching in a solution with 0.4 M H_2O_2 and 4.8 M HF for different times. When the etching time is 5 min, only some sharp tips with a height of ~150 nm could be observed (Figure 4a). As the etching time increases from 5 to 15 min, both the heights and the bottom diameters of the etched nanostructures gradually increase, forming SiNCs (Figure 4a–c). During the top-view SEM investigation of SiNCs, inverted conic holes between Si islands could be observed, as shown in Figure 4d,e. These inverted conic holes imply the gradual reduction of the diameters of Ag particles during the etching process, which results in the diameter increase of SiNCs. These results reflect the catalyst evolution and SiNC-forming process in all-wet MACE.

Forming Mechanism of SiNCs. In a typical MACE procedure, Ag particles contact closely with Si in the etching solution and microscopic galvanic cells are formed (Figure 5a).[27] Ag particles serve as the cathode, while Si is the anode (eqs 1 and 2).[43] When the cathode reaction rate is equal to the anode reaction rate, Ag particles act as catalysts and only Si is etched (eqs 1 and 2), forming SiNWs (Figure 5b).

$$\text{Cathode reaction: } 2H_2O_2 + 4H^+ + 4e^- \rightarrow 4H_2O \quad (1)$$

$$\text{Anode reaction: } Si + 6HF \rightarrow H_2SiF_6 + 4H^+ + 4e^- \quad (2)$$

The diameter of SiNWs is determined by the sizes and distribution of catalysts.[33] However, when the cathode reaction rate is faster than the anode reaction rate, an extra anode reaction of Ag etching can also occur (eq 3).[44,45]

$$Ag \rightarrow Ag^+ + e^- \quad (3)$$

In the SiNC fabrication process, large Ag particles slowed down the anode reaction through hindering the mass transfer of the anode process of Si etching (eq 2), while a high H_2O_2 concentration accelerated the cathode reaction process according to eq 1. The overall anode reaction changed into the simultaneous etching of Si and Ag particles (eqs 2 and 3). As the sizes of Ag particles decrease, the diameters of etched Si nanostructures gradually increase, forming SiNCs (Figure 5c,d). The abovementioned analysis reveals the mechanism of catalyst evolution and diameter control in all-wet MACE fabrication of SiNCs.

Summary of Reaction Conditions for Controlled Fabrication of Si Nanostructures. Based on our exper-

https://doi.org/10.1021/acsomega.1c05790
ACS Omega 2022, 7, 2234–2243

imental results and those reported by others, a diagram showing the relationship between the morphology of Si nanostructures and reaction conditions could be drawn (Figure 6). SiNWs can be obtained in cases that the reaction time is

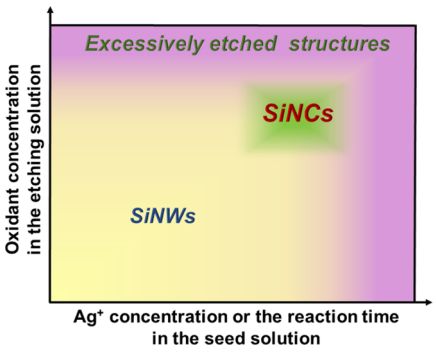

Figure 6. Relationship between the morphology of Si nanostructures and reaction conditions in MACE.

short and the $AgNO_3$ concentration is low in the seed solution, or the oxidant concentration is low in the etching solution. SiNCs could be fabricated at the conditions of appropriately long reaction time and an appropriately high $AgNO_3$ concentration in seed solution, and an appropriately high oxidant concentration in the etching solution. The proper conditions to prepare SiNCs merely fill a very small zone inside the diagram (Figure 6), which may be the reason why SiNCs by the all-wet MACE method have never been reported in the past. This diagram sheds light on the morphology control in MACE processes, which will help to direct the controlled fabrication of various Si nanostructures. Moreover, it is noted that the preparation conditions of Si nanostructures differ by using Si substrates with different doping types and concentrations.[46] The fabrication conditions based on other Si substrates need to be further studied in future work. Despite this, the present diagram may still provide some directions for morphology control of Si nanostructures.

Light Absorption and Photoelectrochemical Property of SiNCs. Furthermore, we compared the light absorption and photoelectrochemical properties of samples with reaction time in seed solution of 120 and 20 s, whose morphologies are SiNCs (Figure 2g) and SiNWs (Figure 2e), respectively. Besides different shapes, the difference in densities and lengths between SiNCs and SiNWs, as well as the cluster formation in SiNWs,[47] may affect the properties, but the comparison can still reflect the property difference for samples with different fabricating conditions. The light absorption spectra of SiNCs, SiNWs, and planar Si were measured by the combination of an integrating sphere, a light source, and a detector, respectively. As shown in Figure 7a, the SiNCs show a stronger light-trapping effect and higher absorption efficiency than SiNWs. The absorption efficiency of SiNCs exceeds 95% at the wavelength range of 300−1000 nm. It is noted that the reabsorption can be eliminated by using our self-building setup (Figure 7b inset) and a specified calibration method,[48] which causes the decrease in measured absorption when compared to that measured with a commercial UV−vis spectrophotometer (PerkinElmer LAMBDA 950) (Figure S10). The reflectivity of SiNCs, SiNWs, and planar Si was also measured with the LAMBDA 950 (Figure S11). It is found that the reflectance of SiNCs is as low as 2% in the visible spectrum.

More importantly, the light absorption of SiNCs exhibits little attenuation when the incident angle increases from 0 to 70° (Figure 7b). In contrast, the light absorption of SiNWs and planar Si decreases with the increase of incident angle. The stable light absorption of SiNCs at different incident angles endows them with great potential in practical solar conversion applications and omnidirectional photodetectors.[49,50] Moreover, compared with SiNWs, the advantage of SiNCs comprises not only a stronger light trapping effect but also reduced surface recombination due to the smaller specific surface area. These merits lead to better photoelectrical properties of SiNCs, as demonstrated in a configuration of liquid-junction solar cells (Figure 7c−e). The SiNW and SiNC cells both show apparent and stable photoresponse with $Me_2Fc^{+/0}$−CH_3OH solution as the electrolyte and a Pt slice as the counter electrode under simulated AM 1.5G solar illumination.[51] Nevertheless, the SiNC cell shows larger open-circuit voltage (−0.27 V) and short-circuit current (2.14 mA cm^{-2}) than the SiNW cell (−0.12 V and 1.80 mA cm^{-2}).

CONCLUSIONS

In conclusion, we report wafer-scale fabrication of SiNCs with the all-wet MACE method. The key is to control the catalyst evolution from deposition to etching stages, which was rationally achieved by changing reaction conditions. In the catalyst deposition process, the sizes of Ag particles increase with the increasing $AgNO_3$ concentration or extending the reaction time in the seed solution. Large-size Ag particles are a necessary condition for fabricating SiNCs. They successively decreased along with the etching of Si in an etching solution with a high H_2O_2 concentration due to the accelerated cathode process and inhibited anode process in Ag/Si microscopic galvanic cells. Thus, the diameter of etched Si nanostructures proportionately increased, forming SiNCs. The obtained SiNC arrays showed more excellent light-trapping effect and photoelectrochemical properties than SiNW arrays. Based on the experimental and reported results, a diagram showing the relationship between the morphology of Si nanostructures and reaction conditions was drawn. SiNCs were fabricated by using n-type 1−10 Ω cm Si(100) wafers in this work. Though the specific experimental conditions for preparing SiNCs may differ by using different Si wafers, the summarized diagram will still provide valuable guidance for morphology control of Si nanostructures in MACE processes. The results deepen the understanding of the MACE mechanism and the new morphology of SiNCs can be applied in optoelectronic devices, catalysts, and sensors. Therefore, our work represents a big progress in morphology control of Si nanostructures, which is important for exploring new properties and applications of Si nanostructures.

EXPERIMENTAL SECTION

MACE Fabrication of Silicon Nanostructures. All samples were prepared from p-type, 4 in. (100) silicon wafers with a resistivity of 1−10 Ω cm. For cleaning samples, the ultrasonic cleaning method was sequentially performed in acetone, ethanol, deionized water, H_2SO_4/H_2O_2 with a 3:1 volume ratio of H_2SO_4 (97%) and H_2O_2 (30%), and deionized water. Then, the wafers were dipped into a solution of HF for 1 min, cleaned with deionized water, and dried with nitrogen.

https://doi.org/10.1021/acsomega.1c05790
ACS Omega 2022, 7, 2234−2243

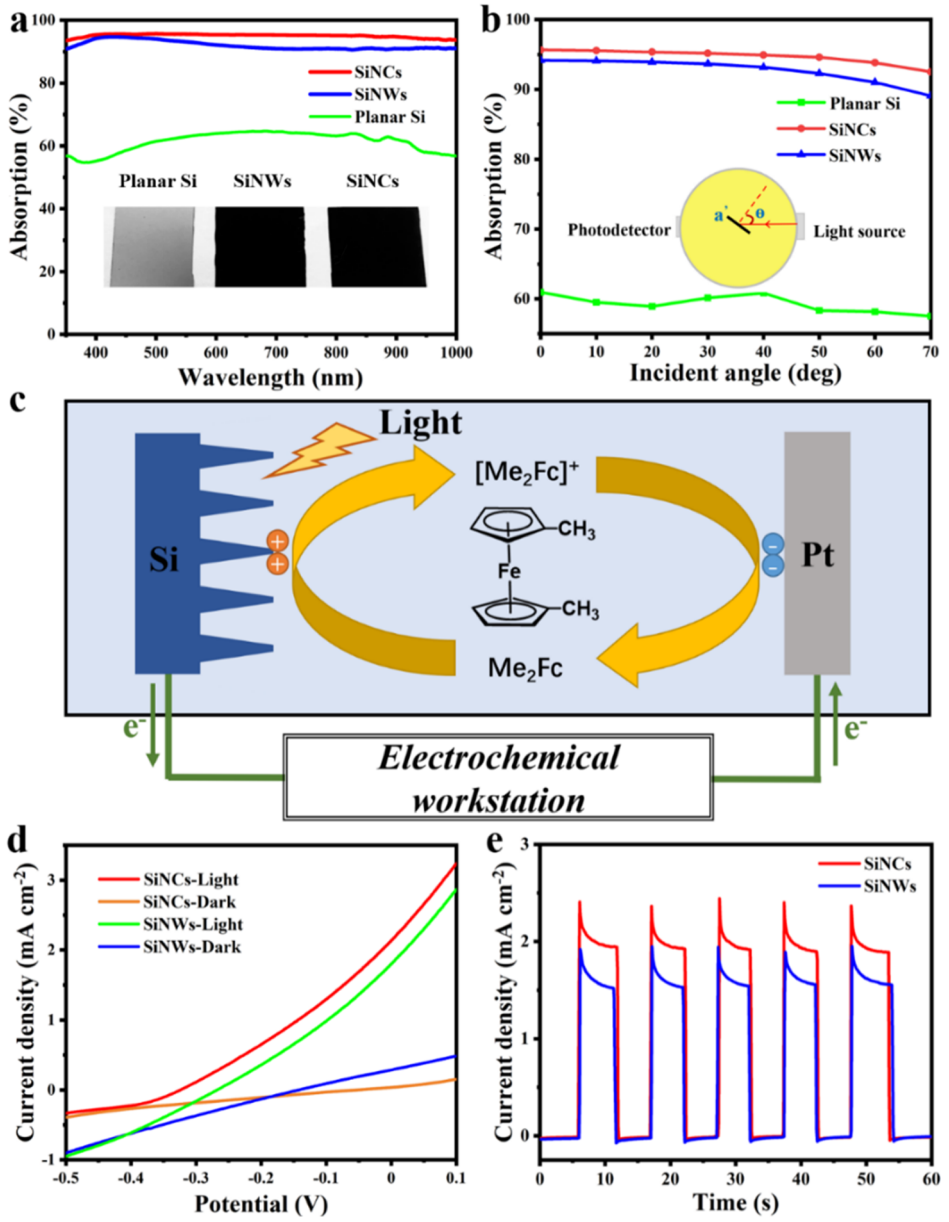

Figure 7. Light absorption and photoelectrochemical properties of various Si nanostructures. (a) Measured light absorption spectra of planar Si, SiNWs, and SiNCs, respectively. Insets are photographs of the samples. (b) Relationship between light absorption efficiencies and incident angles at the wavelength of 488 nm from planar Si, SiNWs, and SiNCs, respectively. The inset shows the measurement setup. (c) Diagram of liquid-junction solar cells based on Si nanostructures. (d) Plots of the current density *vs* the voltage from SiNC and SiNW liquid-junction solar cells in dark and under AM 1.5G solar illumination, respectively. (e) Current densities of SiNC and SiNW liquid-junction solar cells under cycling light on−off switching at 0 bias voltage.

For wafer-scale fabrication of SiNCs, Ag particles were deposited by immersing the cleaned Si wafer in an aqueous seed solution with 0.02 M $AgNO_3$ and 5 M HF for 120 s. Next, the Ag-deposited Si wafer was transferred into an aqueous etching solution with 5 M HF and 0.4 M H_2O_2 and reacted for 15 min. Finally, the sample was soaked in 65% HNO_3 to remove Ag particles and rinsed with deionized water. Sample morphology and structure were characterized by using a SEM instrument (Hitachi, SU5000) and a TEM instrument (FEI TF20).

For the following fabrication, 1.5 cm × 1.5 cm samples cut from Si wafers were adopted.

To study the etching process of SiNCs, the reaction time of the Ag-deposited Si wafer in the etching solution was respectively set as 5, 10, 15, and 60 min, while other conditions were the same as those in the wafer-scale fabrication of SiNCs.

To investigate the influence of Ag particle deposition time, the reaction time in the seed solution was set as 30, 60, 120, and 180 s, while other conditions were the same as those in the wafer-scale fabrication of SiNCs.

To study the influence of H_2O_2 concentration in the etching solution, the H_2O_2 concentration was set as 0.02, 0.2, 0.4, and 0.6 M, while other conditions were the same as those in the wafer-scale fabrication of SiNCs.

Measurement of the Optical Absorption Spectra. The optical beam of a laser-driven light source (EQ-99X) was collimated by an off-axis parabolic mirror, and the diameter of

https://doi.org/10.1021/acsomega.1c05790
ACS Omega 2022, 7, 2234−2243

the beam is suppressed to 2 mm with a telescope system. The beam was sent to an angle-resolved integrating sphere (Labsphere, RTC-060-SF), and the sample was illuminated in the center of the sphere. The scattering light from the sample was collected by a fiber optical spectrometer (Ocean optics, USB2000 + VIS-NIR-ES).

Fabrication and Characterization of Liquid-Junction Solar Cells. First, the SiNW or SiNC sample was adhered to a copper sheet with silver paste. Then, the sample was encapsulated with silicone rubber but a cycle zone of 3 mm diameter was still exposed as the active area. The encapsulated sample was used as the photoelectrode. A CH_3OH solution with 200 mM Me_2Fc, 0.5 mM $[Me_2Fc]BF_4$, and 1 M $LiClO_4$ was used as the electrolyte. A 1 cm × 1 cm Pt slice was used as the counter electrode. The photoelectrochemical performance of the device was tested in a two-electrode configuration with an electrochemical workstation (CHI660E, CH Instruments, Inc.) under simulated AM 1.5G solar illumination.

■ ASSOCIATED CONTENT

Supporting Information

The Supporting Information is available free of charge at https://pubs.acs.org/doi/10.1021/acsomega.1c05790.

SEM images of Si nanostructures and Ag particles, EDX analysis of the sample, examples of the measured cone angles, *L*−*D* relationship of Si nanostructures, diagram of the random Si occupation areas, and absorption and reflection spectrums measured with different equipments (PDF)

■ AUTHOR INFORMATION

Corresponding Authors

Bingchang Zhang − *School of Optoelectronic Science and Engineering, Key Laboratory of Advanced Optical Manufacturing Technologies of Jiangsu Province, Key Laboratory of Modern Optical Technologies of Education Ministry of China, Suzhou 215123, People's Republic of China;* orcid.org/0000-0003-0520-1058; Email: zhangbingchang@suda.edu.cn

Jiansheng Jie − *Institute of Functional Nano & Soft Materials (FUNSOM), Jiangsu Key Laboratory for Carbon-Based Functional Materials & Devices, Soochow University, Suzhou 215123, People's Republic of China; Macao Institute of Materials Science and Engineering, Macau University of Science and Technology, Taipa 999078, People's Republic of China;* orcid.org/0000-0002-2230-4289; Email: jsjie@suda.edu.cn

Xiaohong Zhang − *Institute of Functional Nano & Soft Materials (FUNSOM), Jiangsu Key Laboratory for Carbon-Based Functional Materials & Devices, Soochow University, Suzhou 215123, People's Republic of China;* orcid.org/0000-0002-6732-2499; Email: xiaohong_zhang@suda.edu.cn

Authors

Chenyu Bian − *Institute of Functional Nano & Soft Materials (FUNSOM), Jiangsu Key Laboratory for Carbon-Based Functional Materials & Devices, Soochow University, Suzhou 215123, People's Republic of China*

Zhenghe Zhang − *School of Optoelectronic Science and Engineering, Key Laboratory of Advanced Optical Manufacturing Technologies of Jiangsu Province, Key Laboratory of Modern Optical Technologies of Education Ministry of China, Suzhou 215123, People's Republic of China*

Hui Chen − *School of Optoelectronic Science and Engineering, Key Laboratory of Advanced Optical Manufacturing Technologies of Jiangsu Province, Key Laboratory of Modern Optical Technologies of Education Ministry of China, Suzhou 215123, People's Republic of China*

Dake Zhang − *Institute of Functional Nano & Soft Materials (FUNSOM), Jiangsu Key Laboratory for Carbon-Based Functional Materials & Devices, Soochow University, Suzhou 215123, People's Republic of China*

Shaojun Wang − *School of Optoelectronic Science and Engineering, Key Laboratory of Advanced Optical Manufacturing Technologies of Jiangsu Province, Key Laboratory of Modern Optical Technologies of Education Ministry of China, Suzhou 215123, People's Republic of China;* orcid.org/0000-0002-0812-0782

Jing Ye − *Testing & Analysis Center, Soochow University, Suzhou 215123, People's Republic of China*

Le He − *Institute of Functional Nano & Soft Materials (FUNSOM), Jiangsu Key Laboratory for Carbon-Based Functional Materials & Devices, Soochow University, Suzhou 215123, People's Republic of China;* orcid.org/0000-0002-4520-0482

Complete contact information is available at: https://pubs.acs.org/10.1021/acsomega.1c05790

Notes

The authors declare no competing financial interest.

■ ACKNOWLEDGMENTS

This work was financially supported by the Major Research Plan of the National Natural Science Foundation of China (grant no. 91833303), the Foundation for Innovation Research Groups of the National Natural Science Foundation of China (grant no. 51821002), the Major International (Regional) Joint Research Project of the National Natural Science Foundation of China (grant no. 51920105005), the Natural Science Foundation of Jiangsu Province (nos. BK20200857, BK20200859, and GX2020A05), the National Natural Science Foundation of China (grant no. 62004134), the Entrepreneurship and Innovation Doctor of Jiangsu Province (JSSCBS20210704), Opening Foundation of Jiangsu Key Laboratory for Carbon-Based Functional Materials & Devices, Suzhou Key Laboratory of Functional Nano & Soft Materials, Collaborative Innovation Center of Suzhou Nano Science and Technology, and the Priority Academic Program Development of Jiangsu Higher Education Institutions (PAPD), the 111 Project, and Joint International Research Laboratory of Carbon-Based Functional Materials and Devices.

■ REFERENCES

(1) Wendisch, F. J.; Rey, M.; Vogel, N.; Bourret, G. R. Large-Scale Synthesis of Highly Uniform Silicon Nanowire Arrays Using Metal-Assisted Chemical Etching. *Chem. Mater.* **2020**, *32*, 9425−9434.

(2) Weisse, J. M.; Kim, D. R.; Lee, C. H.; Zheng, X. Vertical Transfer of Uniform Silicon Nanowire Arrays via Crack Formation. *Nano Lett.* **2011**, *11*, 1300−1305.

(3) So, S.; Fung, H. W. M.; Kartub, K.; Maley, A. M.; Corn, R. M. Fabrication of PEDOT Nanocone Arrays with Electrochemically Modulated Broadband Antireflective Properties. *J. Phys. Chem. C* **2017**, *8*, 576−579.

(4) Xu, Z.; Guan, L.; Li, H.; Sun, J.; Ying, Z.; Wu, J.; Xu, N. Structure Transition Mechanism of Single-Crystalline Silicon, G-C_3N_4, and Diamond Nanocone Arrays Synthesized by Plasma Sputtering Reaction Deposition. *J. Phys. Chem. C* **2015**, *119*, 29062−29070.
(5) Jung, J.-Y.; Guo, Z.; Jee, S.-W.; Um, H.-D.; Park, K.-T.; Lee, J.-H. A Strong Antireflective Solar Cell Prepared by Tapering Silicon Nanowires. *Opt. Express* **2010**, *18*, A286−A292.
(6) Peng, K.-Q.; Wang, X.; Wu, X.; Lee, S.-T. Fabrication and Photovoltaic Property of Ordered Macroporous Silicon. *Appl. Phys. Lett.* **2009**, *95*, 143119.
(7) Kim, D. R.; Lee, C. H.; Cho, I. S.; Jang, H.; Jeon, M. S.; Zheng, X. Three-Dimensional Hetero-Integration of Faceted GaN on Si Pillars for Efficient Light Energy Conversion Devices. *ACS Nano* **2017**, *11*, 6853−6859.
(8) Wang, X.; Peng, K.-Q.; Hu, Y.; Zhang, F.-Q.; Hu, B.; Li, L.; Wang, M.; Meng, X.-M.; Lee, S.-T. Silicon/Hematite Core/Shell Nanowire Array Decorated with Gold Nanoparticles for Unbiased Solar Water Oxidation. *Nano Lett.* **2014**, *14*, 18−23.
(9) Kayes, B. M.; Atwater, H. A.; Lewis, N. S. Comparison of the Device Physics Principles of Planar and Radial P-N Junction Nanorod Solar Cells. *J. Appl. Phys.* **2005**, *97*, 114302.
(10) Dong, T.; Sun, Y.; Zhu, Z.; Wu, X.; Wang, J.; Shi, Y.; Xu, J.; Chen, K.; Yu, L. Monolithic Integration of Silicon Nanowire Networks as a Soft Wafer for Highly Stretchable and Transparent Electronics. *Nano Lett.* **2019**, *19*, 6235−6243.
(11) Zhu, J.; Yu, Z.; Burkhard, G. F.; Hsu, C.-M.; Connor, S. T.; Xu, Y.; Wang, Q.; McGehee, M.; Fan, S.; Cui, Y. Optical Absorption Enhancement in Amorphous Silicon Nanowire and Nanocone Arrays. *Nano Lett.* **2009**, *9*, 279−282.
(12) Li, X.; Xiao, Y.; Zhou, K.; Wang, J.; Schweizer, S. L.; Sprafke, A.; Lee, J.-H.; Wehrspohn, R. B. Photoelectrochemical Hydrogen Evolution of Tapered Silicon Nanowires. *Phys. Chem. Chem. Phys.* **2015**, *17*, 800−804.
(13) Wang, K. X.; Yu, Z.; Liu, V.; Cui, Y.; Fan, S. Absorption Enhancement in Ultrathin Crystalline Silicon Solar Cells with Antireflection and Light-trapping Nanocone Gratings. *Nano Lett.* **2012**, *12*, 1616−1619.
(14) Gong, X.; Jiang, Y.; Li, M.; Liu, H.; Ma, H. Hybrid Tapered Silicon Nanowire/PEDOT:PSS Solar Cells. *RSC Adv.* **2015**, *5*, 10310−10317.
(15) Wan, L.; Zhao, Z.; Chen, X.; Liu, P.-F.; Wang, P.; Xu, Z.; Lin, Y.; Wang, B. Controlled Synthesis of Bifunctional $NiCo_2O_4$@FeNi LDH Core−Shell Nanoarray Air Electrodes for Rechargeable Zinc−Air Batteries. *ACS Sustainable Chem. Eng.* **2020**, *8*, 11079−11087.
(16) Wang, C.; Luo, F.; Lu, H.; Rong, X.; Liu, B.; Chu, G.; Sun, Y.; Quan, B.; Zheng, J.; Li, J.; Gu, C.; Qiu, X.; Li, H.; Chen, L. A Well-Defined Silicon Nanocone−Carbon Structure for Demonstrating Exclusive Influences of Carbon Coating on Silicon Anode of Lithium-Ion Batteries. *ACS Appl. Mater. Interfaces* **2017**, *9*, 2806−2814.
(17) Jeong, S.; Garnett, E. C.; Wang, S.; Yu, Z.; Fan, S.; Brongersma, M. L.; McGehee, M. D.; Cui, Y. Hybrid Silicon Nanocone−Polymer Solar Cells. *Nano Lett.* **2012**, *12*, 2971−2976.
(18) Wang, Y.; Lu, N.; Xu, H.; Shi, G.; Xu, M.; Lin, X.; Li, H.; Wang, W.; Qi, D.; Lu, Y.; Chi, L. Biomimetic Corrugated Silicon Nanocone Arrays for Self-Cleaning Antireflection Coatings. *Nano Res.* **2010**, *3*, 520−527.
(19) Wang, Q.; Li, J. J.; Ma, Y. J.; Bai, X. D.; Wang, Z. L.; Xu, P.; Shi, C. Y.; Quan, B. G.; Yue, S. L.; Gu, C. Z. Field Emission Properties of Carbon Coated Si Nanocone Arrays on Porous Silicon. *Nanotechnol* **2005**, *16*, 2919−2922.
(20) Hsu, C.-M.; Connor, S. T.; Tang, M. X.; Cui, Y. Wafer-Scale Silicon Nanopillars and Nanocones by Langmuir−Blodgett Assembly and Etching. *Appl. Phys. Lett.* **2008**, *93*, 133109.
(21) Lu, Y.; Lal, A. High-Efficiency Ordered Silicon Nano-Conical-Frustum Array Solar Cells by Self-Powered Parallel Electron Lithography. *Nano Lett.* **2010**, *10*, 4651−4656.
(22) Zhang, X.; Zhang, J.; Ren, Z.; Li, X.; Zhang, X.; Zhu, D.; Wang, T.; Tian, T.; Yang, B. Morphology and Wettability Control of Silicon Cone Arrays Using Colloidal Lithography. *Langmuir* **2009**, *25*, 7375−7382.
(23) Chen, Y.; Xu, Z.; Gartia, M. R.; Whitlock, D.; Lian, Y.; Liu, G. L. Ultrahigh Throughput Silicon Nanomanufacturing by Simultaneous Reactive Ion Synthesis and Etching. *ACS Nano* **2011**, *5*, 8002−8012.
(24) Jou, S.; Pan, J.-J.; Huang, B.-R. Silicon Nanocone Arrays Deposited by Sputtering. *J. Nanosci. Nanotechnol.* **2009**, *9*, 5927−5931.
(25) Zhang, B.-C.; Wang, H.; He, L.; Zheng, C.-J.; Jie, J.-S.; Lifshitz, Y.; Lee, S.-T.; Zhang, X.-H. Centimeter-Long Single-Crystalline Si Nanowires. *Nano Lett.* **2017**, *17*, 7323−7329.
(26) Hannon, J. B.; Kodambaka, S.; Ross, F. M.; Tromp, R. M. The Influence of the Surface Migration of Gold on the Growth of Silicon Nanowires. *Nature* **2006**, *440*, 69−71.
(27) Huang, Z.; Geyer, N.; Werner, P.; de Boor, J.; Gösele, U. Metal-Assisted Chemical Etching of Silicon: A Review. *Adv. Mater.* **2011**, *23*, 285−308.
(28) Bai, F.; Li, M.; Huang, R.; Li, Y.; Trevor, M.; Musselman, K. P. A One-Step Template-Free Approach to Achieve Tapered Silicon Nanowire Arrays with Controllable Filling Ratios for Solar Cell Applications. *RSC Adv.* **2014**, *4*, 1794−1798.
(29) Huang, Z.; Fang, H.; Zhu, J. Fabrication of Silicon Nanowire Arrays with Controlled Diameter, Length, and Density. *Adv. Mater.* **2007**, *19*, 744−748.
(30) Chang, S.-W.; Chuang, V. P.; Boles, S. T.; Ross, C. A.; Thompson, C. V. Densely Packed Arrays of Ultra-High-Aspect-Ratio Silicon Nanowires Fabricated Using Block-Copolymer Lithography and Metal-Assisted Etching. *Adv. Funct. Mater.* **2009**, *19*, 2495−2500.
(31) Peng, K. Q.; Hu, J. J.; Yan, Y. J.; Wu, Y.; Fang, H.; Xu, Y.; Lee, S. T.; Zhu, J. Fabrication of Single-Crystalline Silicon Nanowires by Scratching a Silicon Surface with Catalytic Metal Particles. *Adv. Funct. Mater.* **2006**, *16*, 387−394.
(32) Huo, C.; Wang, J.; Fu, H.; Li, X.; Yang, Y.; Wang, H.; Mateen, A.; Farid, G.; Peng, K. Q. Metal-Assisted Chemical Etching of Silicon in Oxidizing HF Solutions: Origin, Mechanism, Development, and Black Silicon Solar Cell Application. *Adv. Funct. Mater.* **2020**, *30*, 2005744.
(33) Peng, K.-Q.; Lee, S.-T. Silicon Nanowires for Photovoltaic Solar Energy Conversion. *Adv. Mater.* **2011**, *23*, 198−215.
(34) Sandu, G.; Avila Osses, J.; Luciano, M.; Caina, D.; Stopin, A.; Bonifazi, D.; Gohy, J.-F.; Silhanek, A.; Florea, I.; Bahri, M.; Ersen, O.; Leclère, P.; Gabriele, S.; Vlad, A.; Melinte, S. Kinked Silicon Nanowires: Superstructures by Metal-Assisted Chemical Etching. *Nano Lett.* **2019**, *19*, 7681−7690.
(35) Chen, Y.; Zhang, C.; Li, L.; Tuan, C.-C.; Wu, F.; Chen, X.; Gao, J.; Ding, Y.; Wong, C.-P. Fabricating and Controlling Silicon Zigzag Nanowires by Diffusion-Controlled Metal-Assisted Chemical Etching Method. *Nano Lett.* **2017**, *17*, 4304−4310.
(36) Chen, Y.; Li, L.; Zhang, C.; Tuan, C.-C.; Chen, X.; Gao, J.; Wong, C.-P. Controlling Kink Geometry in Nanowires Fabricated by Alternating Metal-Assisted Chemical Etching. *Nano Lett.* **2017**, *17*, 1014−1019.
(37) Roy, K.; Ghosh, D.; Sarkar, K.; Devi, P.; Kumar, P. Chlorophyll(a)/Carbon Quantum Dot Bio-Nanocomposite Activated Nano-Structured Silicon as an Efficient Photocathode for Photoelectrochemical Water Splitting. *ACS Appl. Mater. Interfaces* **2020**, *12*, 37218−37226.
(38) Qin, Y.; Jiang, Y.; Zhao, L. Modulation of Agglomeration of Vertical Porous Silicon Nanowires and the Effect on Gas-Sensing Response. *Adv. Eng. Mater.* **2018**, *20*, 1700893.
(39) Pinilla, S.; Barrio, R.; González, N.; Pérez Casero, R.; Márquez, F.; Sanz, J. M.; Morant, C. Role of Hydrogen in the Preparation of Amorphous Silicon Nanowires by Metal-Assisted Chemical Etching. *J. Phys. Chem. C* **2018**, *122*, 22667−22674.
(40) Pei, Z.; Hu, H.; Li, S.; Ye, C. Fabrication of Orientation-Tunable Si Nanowires on Silicon Pyramids with Omnidirectional Light Absorption. *Langmuir* **2017**, *33*, 3569−3575.

https://doi.org/10.1021/acsomega.1c05790
ACS Omega 2022, 7, 2234−2243

(41) Chen, C.-Y.; Wei, T.-C.; Lin, C.-T.; Li, J.-Y. Enhancing Formation Rate of Highly-Oriented Silicon Nanowire Arrays with the Assistance of Back Aubstrates. *Sci. Rep.* **2017**, *7*, 3164−3170.
(42) Wu, L.; Li, S.; He, W.; Teng, D.; Wang, K.; Ye, C. Automatic Release of Silicon Nanowire Arrays with a High Integrity for Flexible Electronic Devices. *Sci. Rep.* **2014**, *4*, 3940−3946.
(43) Rajkumar, K.; Pandian, R.; Sankarakumar, A.; Rajendra Kumar, R. T. Engineering Silicon to Porous Silicon and Silicon Nanowires by Metal-Assisted Chemical Etching: Role of Ag Size and Electron-Scavenging Rate on Morphology Control and Mechanism. *ACS Omega* **2017**, *2*, 4540−4547.
(44) Zhang, M.-L.; Peng, K.-Q.; Fan, X.; Jie, J.-S.; Zhang, R.-Q.; Lee, S.-T.; Wong, N.-B. Preparation of Large-Area Uniform Silicon Nanowires Arrays through Metal-Assisted Chemical Etching. *J. Phys. Chem. C* **2008**, *112*, 4444−4450.
(45) Lee, C.-L.; Tsujino, K.; Kanda, Y.; Ikeda, S.; Matsumura, M. Pore Formation in Silicon by Wet Etching Using Micrometre-Sized Metal Particles as Catalysts. *J. Mater. Chem.* **2008**, *18*, 1015−1020.
(46) Pinna, E.; Le Gall, S.; Torralba, E.; Mula, G.; Cachet-Vivier, C.; Bastide, S. Mesopore Formation and Silicon Surface Nanostructuration by Metal-Assisted Chemical Etching with Silver Nanoparticles. *Front. Chem.* **2020**, *8*, 658.
(47) Romano, L.; Kagias, M.; Vila-Comamala, J.; Jefimovs, K.; Tseng, L.-T.; Guzenko, V. A.; Stampanoni, M. Metal Assisted Chemical Etching of Silicon in the Gas Phase: A Nanofabrication Platform for X-ray Optics. *Nanoscale Horiz.* **2020**, *5*, 869−879.
(48) de Mello, J. C.; Wittmann, H. F.; Friend, R. H. An Improved Experimental Determinationof External Photoluminescence Quantum Efficiency. *Adv. Mater.* **1997**, *9*, 230−232.
(49) Putra, I. R.; Li, J.-Y.; Chen, C.-Y. 18.78% Hierarchical Black Silicon Solar Cells Achieved with the Balance of Light-Trapping and Interfacial Contact. *Appl. Surf. Sci.* **2019**, *478*, 725−732.
(50) Huang, Y.-F.; Chattopadhyay, S.; Jen, Y.-J.; Peng, C.-Y.; Liu, T.-A.; Hsu, Y.-K.; Pan, C.-L.; Lo, H.-C.; Hsu, C.-H.; Chang, Y.-H.; Lee, C.-S.; Chen, K.-H.; Chen, L.-C. Improved Broadband and Quasi-Omnidirectional Anti-Reflection Properties with Biomimetic Silicon Nanostructures. *Nat. Nanotechnol.* **2007**, *2*, 770−774.
(51) Santori, E. A.; Maiolo III, J. R.; Bierman, M. J.; Strandwitz, N. C.; Kelzenberg, M. D.; Brunschwig, B. S.; Atwater, H. A.; Lewis, N. S. Photoanodic Behavior of Vapor-Liquid-Solid−Grown, Lightly Doped, Crystalline Si Microwire Arrays. *Energy Environ. Sci.* **2012**, *5*, 6867−6871.

https://doi.org/10.1021/acsomega.1c05790
ACS Omega 2022, 7, 2234−2243